DOI: 10.1002/ejic.201100234

Oxygen-Deficient $R_2MoO_{6-\delta}$ (R = Tb, Dy, Y, Ho, Er, Tm, Yb) with Fluorite Structure as Potential Anodes in Solid Oxide Fuel Cells

A. Aguadero,*[a] M. J. Martínez-Lope,[a] V. Pomjakushin,[b] and J. A. Alonso[a]

Keywords: Fluorites / Lanthanides / Fuel cells / Molybdenum / Oxides

The members of the family of oxygen-defective fluorites $R_2MoO_{6-\delta}$ (R = Tb, Dy, Y, Ho, Er, Tm, Yb) have been synthesized under reducing conditions and characterized in order to evaluate their potential use as anodes in intermediate-temperature solid oxide fuel cells (IT-SOFCs). A neutron powder diffraction (NPD) investigation demonstrates that they are all cubic, in the $Fm\bar{3}m$ space group, exhibiting a random distribution of R and Mo cations over the metal sites of the fluorite structure with crystallographic formula $MO_{2-\delta/3}$ ($M = R_{2/3}Mo_{1/3}$), Z = 4. These materials are highly oxygen-deficient fluorites with oxygen stoichiometries ranging from 5.2(1) (R = Y, Tm) to 4.8(1) (R = Tb, Dy, Ho, and Er) oxygen atoms per formula unit, accompanied by high values of the displacement parameters at room temperature (ca. 5 Å^2), which suggests a high mobility of the oxygen atoms. An in situ NPD study of the thermal evolution of the crystal structure for $Ho_2MoO_{6-\delta}$ confirms the absence of phase transitions and a high oxygen-vacancy concentration and mobility [B(O) = 6.7(1) Å^2] in the network under the usual working conditions of an anode in a SOFC ($P_{O2} \approx 10^{-6}$ Torr, 500–700 °C). The thermal expansion coefficients of the sintered samples exhibit values around 9×10^{-6} K^{-1} from 300 to 900 °C under 5 % H_2/95 %N_2, which perfectly match the thermal expansions of the other components of a SOFC. The maximum conductivity values are displayed for the fluorite containing Tb, ranging from 0.03 (200 °C) to 1.1 (900 °C) S cm^{-1} with an activation energy of 0.31 eV.

Introduction

Solid oxide fuel cells (SOFCs) are solid-state devices that drive the electrochemical oxidation of a fuel (typically H_2) with an oxidant (typically O_2 from the air) to yield clean electrical energy with H_2O as the only byproduct. State-of-the-art SOFC devices work at elevated temperatures around 1000 °C, which is extremely demanding for the different components, cathode, anode, electrolyte, and interconnects. Nowadays, the development of an adequate anode material for intermediate-temperature solid oxide fuel cells (IT-SOFC), which functions below 800 °C, is of great interest. The target is a mixed ionic/electronic conductor that is stable in the anodic atmosphere and has high catalytic activity for fuel oxidation and tolerance to sulfur poisoning.

Mo-based oxides have been found to have an excellent tolerance to sulfur.[1] Among them, the family of R_2MoO_6 molybdates (R = rare earths or Bi) displays appealing catalytic properties in the oxidation of hydrocarbons. For instance, Bi_2MoO_6 is an extensively used catalytic component for selective olefin oxidation;[2] La_2MoO_6 and Pr_2MoO_6[3–5] have also been described as catalysts in the selective oxidation of toluene and isobutene, respectively. Moreover, a related compound, $La_2Mo_2O_9$, was reported to be a fast oxide-ion conductor with an ionic conductivity of 6×10^{-2} S cm^{-1} at 800 °C, comparable with other widely used solid oxide fuel cell electrolytes.[6] Depending on their size or the synthesis conditions, the compounds of the R_2MoO_6 series have been described to crystallize in the monoclinic (α), cubic (β), or tetragonal (γ) polymorphs.[7,8] In a previous publication, we reported new α-R_2MoO_6 polymorphs for the small-sized rare earths, R = Y, Dy, Ho, Er, Tm, Yb,[9] defined in the monoclinic $C2/c$ space group, as well as a new cubic phase for R = Pr of actual stoichiometry $Pr_5Mo_3O_{16}$.[10]

Mo^{IV}-containing oxides have been described to present very different physical properties as a function of the crystal structure and the presence or absence of Mo clusters of different sizes in the lattice. Manthiram and Goppalakrishnan[11] observed that the controlled reduction of R_2MoO_6 leads to the formation of a monoclinic Yb_2ReO_5-type structure for R = La, Pr, and Nd, whereas a cubic fluorite-type structure was obtained for R = Gd, Tb, Dy, and Ho. Later on, the stabilization of a cubic fluorite structure was achieved for La_2MoO_5 that shows a semiconductor–metal transition at 250 °C and a paramagnetic behavior below this transition.[11,12] No details on the crystal structures of these reduced phases were given.

This paper reports on the preparation of polycrystalline samples and a comprehensive crystal structure study of the $R_2MoO_{6-\delta}$ polymorphs for small-sized rare earths, R = Tb,

[a] Instituto de Ciencia de Materiales de Madrid, C.S.I.C., Cantoblanco, 28049 Madrid, Spain
E-mail: ainara.aguadero@icmm.csic.es
[b] Laboratory for Neutron Scattering, ETH Zurich and PSI Villigen, 5232 Villigen PSI, Switzerland

Dy, Y, Ho, Er, Tm, and Yb. In order to determine the structural features, in particular the oxygen content and possible long-range ordering of the oxygen vacancies, neutron powder diffraction[13] was used, for the first time, as a tool to characterize these oxides. This analysis is enlightening in the sense that the distribution of the oxygen atoms over high-multiplicity sites with large displacement factors gives an important hint on the possible oxide-ion conductivity in these materials, which is essential in their role as anodes in SOFCs. Moreover, the thermal expansion and electrical properties of selected samples are also important for this role.

Results and Discussion

Crystallographic Characterization

Reduced $R_2MoO_{6-\delta}$ (R = Y, Dy, Ho, Er, Tm, Yb) oxides were synthesized as pure and well-crystallized powders, as checked by XRD diffraction measurements. Figure 1 shows the XRD patterns obtained for each compound; all of them are characteristic of single-phase fluorite oxides. The neutron powder diffraction data at room temperature were successfully refined in the cubic $Fm\bar{3}m$ space group, No. 225. The absence of superstructure peaks with respect to the ideal fluorite structure, with $a_0 \approx 5.2$ Å, suggests that R and Mo are distributed at random over the metal positions of the fluorite. In fact, $R_2MoO_{6-\delta}$ must be rewritten as $R_{2/3}Mo_{1/3}O_{2-\delta/3}$, indicating a defective MO_2 fluorite, with $Z = 4$ in the $Fm\bar{3}m$ space group (we will keep the $R_2MoO_{6-\delta}$ nomenclature hereafter for consistency). In the simple fluorite structural model, 2/3 R and 1/3 Mo cations are randomly distributed over the 4*a* (0,0,0) sites, and the oxygen atoms at the 8*c* (1/4,1/4,1/4) positions. The refinement of the oxygen occupancy factor demonstrated the presence of a significant number of oxygen vacancies (Table 1). The oxygen stoichiometries range from 5.2(1) (R = Y, Tm) to 4.8(1) (R = Tb, Dy, Ho, and Er) in $R_2MoO_{6-\delta}$; therefore, δ spans the range from 0.8(1) to 1.2(1). Figure 2 illustrates the goodness of the NPD fit for $Tb_2MoO_{6-\delta}$ and $Yb_2MoO_{6-\delta}$. Table 1 lists the unit cell parameters and reliability factors for each refinement. A regular variation of the unit cell parameters and interatomic distances is observed with the ionic radii of the rare-earth cations,[14] according to the well-known lanthanide contraction, as displayed in Figure 3, except for the Y compound, which presents a smaller volume than expected from the tabulated ionic radius. The final atomic coordinates, isotropic displacement factors, and bonding distances after the refinement are listed in Table 1.

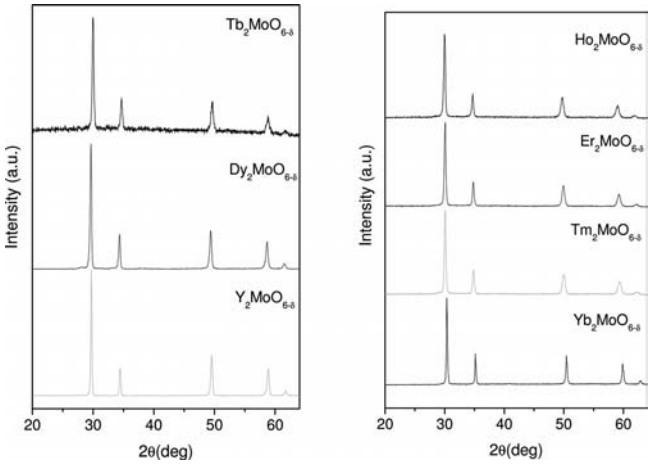

Figure 1. X-ray diffraction patterns for $R_2MoO_{6-\delta}$.

Table 1. Lattice, atomic, and displacement parameters for $R_2MoO_{6-\delta}$ (R = Tb, Dy, Y, Ho, Er, Tm, Yb), defined in the cubic $Fm\bar{3}m$ space group, (structural formula $R_{2/3}Mo_{1/3}O_{2-\delta/3}$, $Z = 4$), from NPD data at 295 K. Reliability factors after the Rietveld refinement are also given.

R	Tb	Dy	Y	Ho	Er	Tm	Yb
a (Å)	5.252(1)	5.2262(5)	5.2066(2)	5.2129(6)	5.1915(9)	5.1787(9)	5.1601(6)
V (Å^3)	144.89(5)	142.75(2)	141.141(9)	141.66(3)	139.92(4)	138.88(4)	137.39(3)
(R,Mo) 4*a* (0 0 0)							
B (Å^2)	1.75(4)	1.66(2)	1.64(4)	1.80(3)	1.48(7)	1.55(4)	1.78(3)
f_{occ} (R)	0.667	0.667	0.667	0.667	0.667	0.667	0.667
f_{occ} (Mo)	0.333	0.333	0.333	0.333	0.333	0.333	0.333
O 8*c* (1/4,1/4,1/4)							
B (Å^2)	5.3(1)	4.5(1)	5.0(1)	4.7(8)	4.49(2)	5.1(1)	4.45(9)
f_{occ}	0.80(2)	0.79(2)	0.86(2)	0.80(2)	0.79(2)	0.87(1)	0.84(1)
Reliability factors							
R_p	2.86	1.46	3.99	1.61	3.15	2.22	2.29
R_{wp}	3.67	1.86	5.43	2.11	4.00	2.82	2.93
R_{exp}	2.80	1.10	2.20	1.08	3.30	2.09	2.08
χ^2	1.72	2.85	6.09	3.79	1.46	1.82	1.99
R_{Bragg}	5.81	3.78	3.44	4.20	2.12	3.92	1.93
Interatomic distances (Å)							
(R,Mo)–O	2.2743(3)	2.2630(1)	2.2545(5)	2.2573(2)	2.2480(2)	2.2424(2)	2.2344(2)

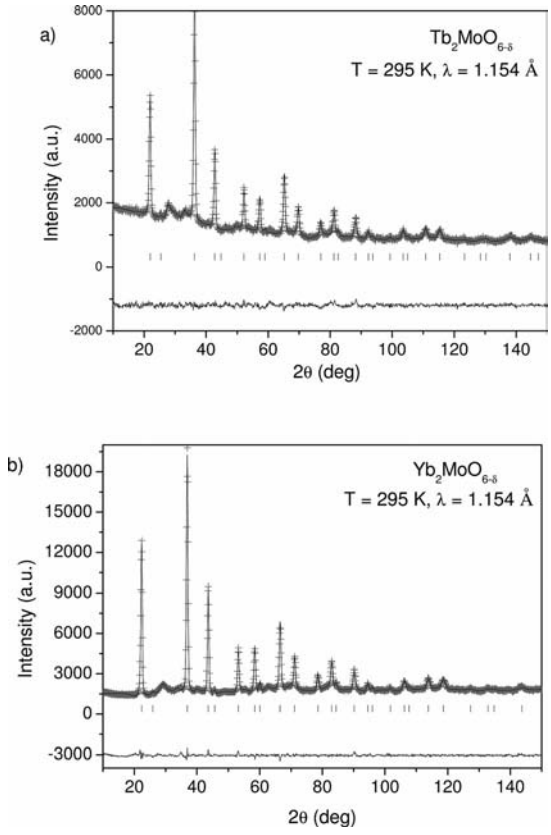

Figure 2. Observed (crosses), calculated (solid line), and difference (bottom) NPD Rietveld profiles for (a) $Tb_2MoO_{6-\delta}$ and (b) $Yb_2MoO_{6-\delta}$ at 295 K.

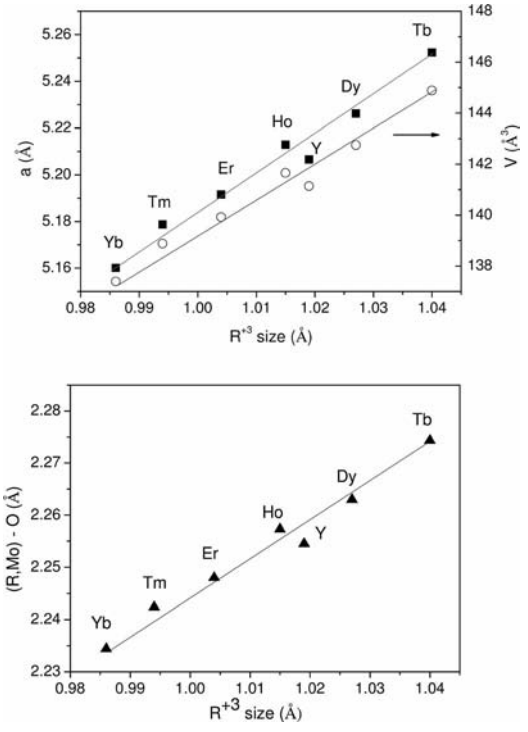

Figure 3. Evolution of the (a) unit cell parameters and (b) bond lengths of the $R_2MoO_{6-\delta}$ series with the R^{3+} ionic radius.

Up to now, the oxygen-deficient fluorites described for the heavier rare-earth elements (R = Gd, Tb, Dy, and Ho) were assumed to present a R_2MoO_5 stoichiometry with an oxidation state of +4 for Mo. However, the refinement of the oxygen occupancy factors provides evidence that these materials present a variable deficiency with oxygen stoichiometries ranging from 5.2(1) to 4.8(1), with no apparent variation of the oxygen content with the rare-earth ionic radius. On the other hand, the high oxygen-vacancy concentration is accompanied by high values of the isotropic displacement parameters at room temperature (ca. 5 $Å^2$), which could indicate a high mobility of the oxygen atoms. These high isotropic thermal displacement parameters, together with the irregular background observed in our samples, were also described in the LAMOX family and associated with a substantial disorder of the oxygen sublattice responsible for the high oxygen mobility displayed by these compounds.[15]

On the other hand, the obtained oxygen stoichiometries suggest a mixed-valence state for the Mo ions between +3 and +4 for $\delta > 1$ and between +4 and +5 for $\delta < 1$ in $R_2MoO_{6-\delta}$, which could induce some electronic conductivity in these materials by polaron hopping. In the simple fluorite crystal structure, there is a single (R,Mo)–O distance corresponding to the cubic $(R,Mo)O_8$ coordination groups. In our case, the oxygen deficiency implies the decrease of the coordination number of the metal atoms to average values in the range $(R,Mo)O_6$–$(R,Mo)O_7$.

The thermal evolution of the crystal structure of the $Ho_2MoO_{6-\delta}$ member was studied by in situ NPD. The crystal structure was successfully refined in the cubic $Fm\bar{3}m$ space group in all the measured temperature range, and no segregation of impurities or phase transitions was observed. Figure 4 illustrates the goodness of the fit for the pattern collected at 700 °C. The temperature-dependent NPD data also allowed the determination of the expansion of the lattice. The unit cell parameter expands from 5.2129(6) Å at 295 K to 5.2349(2) Å at 823 K and to 5.2426(2) at 973 K,

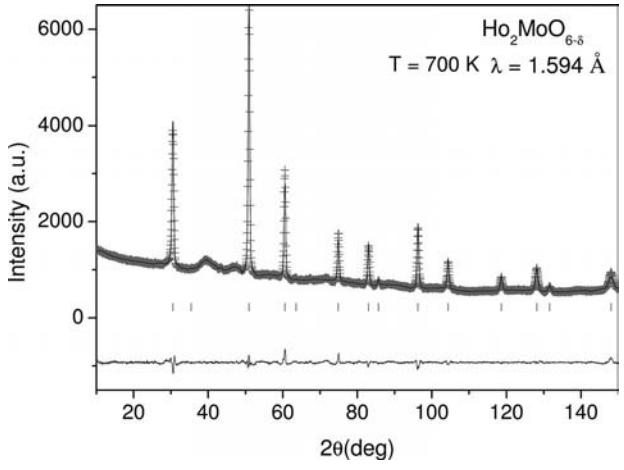

Figure 4. Observed (crosses), calculated (solid line), and difference (bottom) NPD Rietveld profiles for $Ho_2MoO_{6-\delta}$ at 700 °C under vacuum.

leading to an expansion coefficient of 8.45×10^{-6} K^{-1} between 295 and 973 K for R = Ho. The oxygen stoichiometry in the measured temperature range does not vary perceptibly between 823 [4.98(6)] and 973 K [4.92(6)], with a slight increase in the isotropic displacement factors from 6.4(1) to 6.7(1) $Å^2$ for 823 and 973 K, respectively. The increase in the isotropic displacement parameters suggests higher oxygen mobility at higher temperatures, as expected. At these temperatures, the average oxidation state of Mo is found to be close to +4 in the measurement environment ($P_{O2} \approx 10^{-6}$ Torr). Figure 5 illustrates the oxygen-defective fluorite structure, in which some atoms have been randomly removed from the oxygen sublattice; the arrows suggest the motion of O atoms, which diffuse by an oxygen-vacancy mechanism.

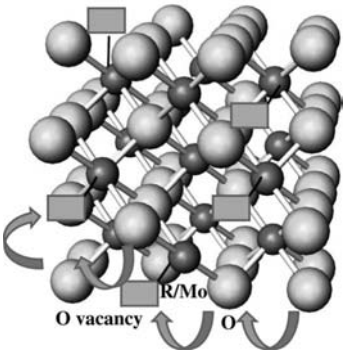

Figure 5. Representation of the cubic fluorite crystal structure; small and large atoms stand for (R,Mo) and O, respectively. Some oxygen atoms have been randomly removed to indicate the defective character of the structure. Rectangles stand for oxygen vacancies.

The oxygen content was also evaluated by thermogravimetric analysis under an O_2 flow in order to determine the oxygen intake during the oxidation processes of the reduced phases $R_2MoO_{6-\delta}$ to the oxidized phases R_2MoO_6. Figure 6 illustrates, for R = Ho, that the oxygen deficiency values (δ) are around 1 oxygen atom per formula unit, as determined by NPD. After the oxidation process, taking place between approximately 500 and 800 °C, the XRD diagram of the product corresponds to monoclinic Ho_2MoO_6,[9] containing Mo^{6+} ions.

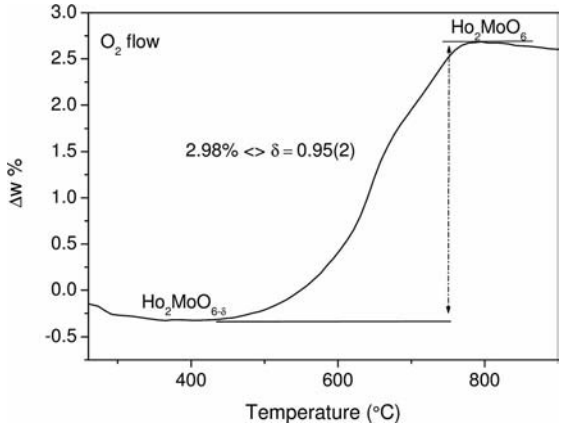

Figure 6. Thermogravimetric curves under O_2 flow for $Ho_2MoO_{6-\delta}$.

Thermal Expansion

For the measurement of the thermal expansion, we selected three samples, Tb with the highest ionic radius, Yb with the lowest, and Ho with an intermediate ionic radius. The measurements from 35 to 900 °C in a 5%H_2/95%N_2 flow shows a linear behavior for R = Ho and Yb and no abrupt transitions in the entire temperature range measured. However, for $Tb_2MoO_{6-\delta}$, a sudden contraction is observed at around 800 °C (Figure 7). This discontinuity could be related to an electron transfer from Tb to Mo. For all the samples, a decrease in the slope is observed at around 300 °C. Table 2 contains the thermal expansion coefficient (TEC) values for the studied oxides in the temperature ranges below and above 300 °C. The TECs of the sintered samples exhibit values around 9×10^{-6} K^{-1} in the high-temperature region, which perfectly match the thermal expansions of the other components of a SOFC.[16] The coefficient for $Ho_2MoO_{6-\delta}$ obtained by neutron power diffraction measurements (8.45×10^{-6} K^{-1}) is in good agreement with that determined by dilatometric analysis (8.75×10^{-6} K^{-1}) in the high-temperature range.

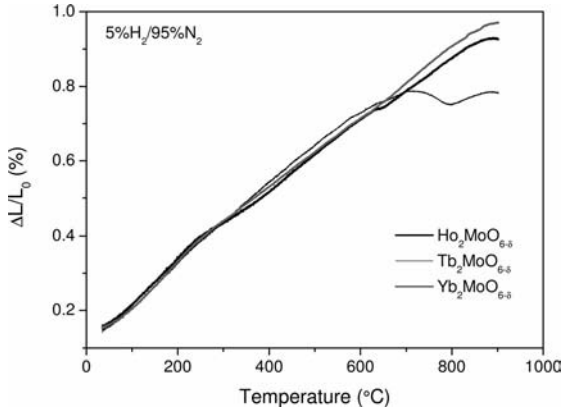

Figure 7. Thermal expansion for the $R_2MoO_{6-\delta}$ system under 5% H_2/95% N_2 flow.

Table 2. Thermal expansion coefficients (TEC) for $R_2MoO_{6-\delta}$.

R	TEC $_{35–300\ °C} \times 10^6$ K^{-1}	TEC $_{300–900\ °C} \times 10^6$ K^{-1}
Tb	12.3 (1)	10.0(1)
Ho	14.9 (1)	8.7 (1)
Yb	12.5 (1)	9.2 (1)

Electrical Conductivity

The electrical conductivity was measured for $Tb_2MoO_{6-\delta}$, with 4.8(1) oxygen atoms per formula unit and an expected mixed Mo^{3+}/Mo^{4+} oxidation state, and for $Yb_2MoO_{6-\delta}$, with 5.0(1) oxygen atoms per formula unit and an average oxidation state for Mo close to 4+. It is impor-

tant to note that the densification of the pellets was complicated due to the limitation of the sintering temperature to 900 °C, in order to avoid the segregation of secondary phases, as described previously. Figure 8 shows a semiconductor-like behavior for both Yb and Tb samples. The maximum conductivity values are measured for the Tb fluorite with conductivity values that range from 0.03 Scm^{-1} (200 °C) to 1.1 Scm^{-1} (900 °C); in this sample, a slight change in the slope is also observed at temperatures higher than 800 °C, which could be related to the electron transfer between Tb and Mo, which was previously related to the discontinuity in the thermal expansion curve (Figure 7). The activation energies for the two samples are quite similar with values of 0.31 eV for $Tb_2MoO_{6-\delta}$ and 0.35 eV for $Yb_2MoO_{6-\delta}$ over the measured temperature range and comparable to those reported[11] (0.2–0.3 eV) for cubic R_2MoO_5 in the temperature range 300–720 K.

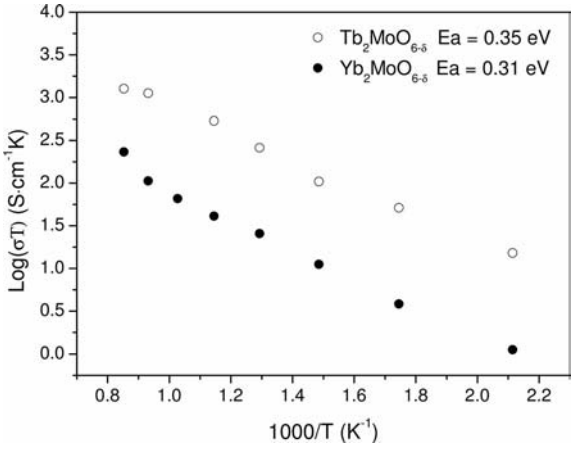

Figure 8. Thermal variation of the electrical conductivity under 5% H_2/95% N_2 flow.

With two-point ac impedance measurements, we are able to obtain the total conductivity of the samples as the sum of the ionic and the electronic conductivity. In these samples, the relatively high values of electrical conductivities obtained, up to 1.1 Scm^{-1}, and the low activation energies should be associated with a greater contribution of the electronic conductivity that masks the ionic contribution. Ionic conductivities below 0.1 Scm^{-1} at 800 °C {measured for $La_{0.8}Sr_{0.2}Ga_{0.83}Mg_{0.17}O_{2.815}$ (LSGM), one of the best ionic conductors at intermediate temperatures[17]} are usually monitored. It is important to note that both ionic and electronic contributions are essential for SOFC anode materials.

The electronic conductivity in these oxides is expected to occur by a thermally activated polaron-hopping mechanism. Actually, the higher electronic conductivity of the Tb sample must be related to the mixed oxidation state of Mo, which could favor the polaron hopping across Mo^{3+}–O–Mo^{4+} paths. The random distribution of 2/3 R and 1/3 Mo over the metal positions certainly hinders the conduction pathways; despite this impediment, the total conductivity reaches 1.04 Scm^{-1} at 800 °C, which is of the required magnitude for SOFC anodes[18] as argued by Atkinson et al.

The large electronic contribution prevents the evaluation of the ionic contribution in these materials. However, the considerable oxygen-vacancy concentration and thermal displacements in these highly disordered phases suggests a sizeable oxygen mobility, as previously observed in other Mo fast-ionic conductors.[19] Good oxide ion conductivity requires the partial occupancy of an energetically equivalent set of oxide ion lattice sites, such as the anion sites of the fluorite structure.[20] In fact, some of the best oxide ion conductors exhibit a defective fluorite structure, like rare-earth-doped CeO_2 or cubic-stabilized zirconia, $Zr_{1-x}Y_xO_{2-x/2}$, where the host cations (Ce^{4+} or Zr^{4+}) are replaced by lower-valent R^{3+}cations. The missing charge is balanced by the formation of oxygen vacancies in the oxide ion sublattice, resulting in an impressive conductivity. In the present case, the defective fluorite of stoichiometry $R_2MoO_{6-\delta}$ is achieved by the reduction of Mo^{6+} to lower oxidation valences close to 4+, creating about one oxygen vacancy per formula unit. The large displacement factors observed at the oxygen sublattice, indicating a smearing of the nuclear density (observed by neutron diffraction) suggest a high mobility of the oxygen atoms by hopping to adjacent oxygen vacancies (Figure 5). On the other hand, the reduction of the Mo oxidation state is also responsible for a significant electronic conduction. These materials are thus expected to present mixed ionic/electronic conductivity, being potentially useful as anodes for IT-SOFCs.

Conclusions

A series of oxygen-defective fluorites with composition $R_2MoO_{6-\delta}$ (R = Tb, Dy, Y, Ho, Er, Tm, Yb; $\delta \approx 1$) has been prepared and characterized; some of them (Er, Tm, and Yb) are described for the first time. The crystal structure can be defined in a simple-cubic fluorite cell, space group $Fm\bar{3}m$, with crystallographic formula $MO_{2-\delta/3}$ ($M = R_{2/3}Mo_{1/3}$), $Z = 4$, as demonstrated by NPD data. R and Mo are distributed at random over the metal positions. The significant oxygen deficiency and oxygen thermal displacements suggest elevated oxygen mobility in these materials. In situ NPD data of $Ho_2MoO_{6-\delta}$ inside a furnace simulating the usual working conditions of an anode in a SOFC ($P_{O2} \approx 10^{-6}$ Torr, 500–700 °C) show the absence of phase transitions or segregation of secondary compounds. The electrical conductivity displays a semiconducting-like behavior suggesting electronic conduction by the polaron-hopping mechanism. The maximum conductivity value was observed for the Tb compound, in which the mixed oxidation state of Mo favors the hopping across Mo^{3+}–O–Mo^{4+} paths, exhibiting a value of σ = 1.04 Scm^{-1} at 800 °C, as required for an anode material in SOFCs. These disordered fluorites are expected to present mixed ionic/electronic conductivity with TEC values that perfectly match those of the usual SOFC electrolytes, and they are therefore presented as potential anodes for SOFCs.

Experimental Section

Polycrystalline $R_2MoO_{6-\delta}$ (R = Y, Dy, Ho, Er, Tm, Yb) samples were prepared by solid state reaction, from stoichiometric amounts of analytical grade R_2O_3 and MoO_3. The reactants were mixed, ground, and calcined at 1150 °C for 12 h in air. Afterwards, the resulting powders were treated in an H_2/N_2 (5%/95%) flow at 900° for 12 h. Higher heating temperatures lead to the formation of $R_2Mo_5O_{12}$ and R_2O_3. However, it is important to note that for IT-SOFCs the operating temperature range is between 550 and 850 °C, in which the samples are perfectly stable.

The initial characterization of the products was carried out by laboratory X-ray diffraction (XRD) (Cu-K_α, λ = 1.5406 Å). Neutron powder diffraction (NPD) diagrams were collected at the HRPT diffractometer[21] of the SINQ spallation source, at ETH-Zurich. The patterns were collected at room temperature with a wavelength of 1.154 Å. The high-flux mode was used; the collection time was 2 h, except for the absorbing $Dy_2MoO_{6-\delta}$ sample, collected in 9 h. A vanadium can with a 6 mm diameter was used; for $Dy_2MoO_{6-\delta}$ a double-walled vanadium sample holder was employed to minimize absorption. All the patterns were refined by the Rietveld method,[22] with the FULLPROF refinement program.[23] A pseudo-Voigt function was chosen to generate the line shape of the diffraction peaks. The following parameters were refined in the final runs: scale factor, background coefficients, zero-point error, pseudo-Voigt correction for asymmetry parameters, positional coordinates, and isotropic thermal factors. The absorption of the $R_2MoO_{6-\delta}$ samples was measured, and μ_R values of 0.399, 0.399, 0.164, 0.308, 0.151 for R = Tb, Dy, Ho, Er, and Tm, respectively, were considered during the refinement. The coherent scattering lengths for Tb, Dy, Y, Ho, Er, Tm, Yb, Mo, and O were 7.38, 16.9, 7.75, 8.01, 7.79, 7.07, 12.4, 6.72, and 5.803 fm, respectively.

For $Ho_2MoO_{6-\delta}$ the thermal evolution of the crystal structure was evaluated by NPD at the D2B diffractometer of the Institute Laue-Langevin, Grenoble (France). A wavelength of λ = 1.594 Å was selected from a Ge monochromator. In this study, the usual working environment of an anode in an IT-SOFC was simulated in the temperature range 500–700 °C under vacuum ($P_{O2} \approx 10^{-6}$ Torr).

The oxygen content was also evaluated by thermogravimetric analysis with a Mettler TA3000 system equipped with a TC10 processor unit. Thermogravimetric (TG) curves were obtained with a TG50 unit, working at a heating rate of 10 °C min^{-1}, in an O_2 flow of 0.3 L min^{-1}.

Dense compounds were required in order to evaluate the thermal expansion and electrical conductivity. For this purpose, the powders were uniaxially pressed (ca. 1 Ton) to produce cylindrical pellets. The reduced $R_2MoO_{6-\delta}$ powders were sintered at 900 °C for 6 h in a 5% H_2/N_2 atmosphere in order to avoid the formation of secondary phases. We experienced severe problems in the preparation of dense samples due to the limitation of the sintering temperature at 900 °C.

The thermal expansion coefficients were determined by dilatometric analysis with a Linseis L75/1550C dilatometer under 5% H_2/N_2 flow. The measurement of each sample was repeated four times in order to ensure reproducibility. A two-electrode configuration was used to measure the electrical conductivity under reducing conditions between 25 and 900 °C ac impedance spectroscopy. For this purpose, two Pt wires were attached to the bars, and they were fixed with Pt ink (Fuel-cell-materials) to ensure good electrical contact. Ac impedance analysis was performed, in the range 10^{-1}–10^6 Hz, with an excitation voltage of 10 mV by using an AUTOLAB PGSTAT 302, ECO CHEMIE instrument. The two-point ac impedance conductivity was measured in disks of 0.22 cm^2 area and 0.16 cm thickness for $Tb_2MoO_{6-\delta}$ and of 0.24 cm^2 area and 0.29 cm thickness for $Yb_2MoO_{6-\delta}$.

Acknowledgments

This work was sponsored by the Innovation and Science Ministry (MAT2010–16404). A. A. is grateful to this Ministry for financial support ("Juan de la Cierva" program). This work is partially based on the results of experiments carried out at the Swiss spallation neutron source SINQ, Paul Scherrer Institut, Villigen, Switzerland.

[1] Y. H. Huang, R. I. Dass, Z. L. Xing, J. B. Goodenough, *Science* **2006**, *312*, 254–257.
[2] D. J. Buttrey, T. Vogt, U. Wildgruber, W. R. Robinson, *J. Solid State Chem.* **1994**, *111*, 118–127.
[3] D. D. Agarwal, K. L. Madhok, H. S. Goswami, *React. Kinet. Catal. Lett.* **1994**, *52*, 225–232.
[4] F. De Smet, M. Devillers, C. Poleunis, P. Bertrand, *J. Chem. Soc. Faraday Trans.* **1998**, *94*, 941–947.
[5] F. De Smet, P. Ruiz, B. Delmon, M. Devillers, *J. Phys. Chem. B* **2001**, *105*, 12355–12363.
[6] P. Lacorre, F. Goutenoire, O. Bohnke, R. Retoux, Y. Laligant, *Nature* **2000**, *404*, 856–858.
[7] P. V. Klevtsov, L. Y. Kharchenko, R. F. Kleftsova, *Sov. Phys. Crystallogr.* **1975**, *20*, 349.
[8] L. H. Brixner, A. W. Sleight, M. S. Licis, *J. Solid State Chem.* **1972**, *5*, 186–190.
[9] J. A. Alonso, F. Rivillas, M. J. Martinez-Lope, V. Pomjakushin, *J. Solid State Chem.* **2004**, *177*, 2470–2476.
[10] M. J. Martínez-Lope, J. A. Alonso, D. Sheptyakov, V. Pomjakushin, *J. Solid State Chem.* **2010**, *183*, 2974–2978.
[11] A. Manthiram, J. Gopalakrishnan, *J. Less Common Metals* **1984**, *99*, 107–111.
[12] F. Shi, Y. Ren, *Solid State Commun.* **1995**, *95*, 745–747.
[13] J. A. Alonso, M. J. Martínez-Lope, A. Aguadero, L. Daza, *Prog. Solid State Chem.* **2008**, *36*, 134–150.
[14] R. D. Shannon, *Acta Crystallogr., Sect. A* **1976**, *32*, 751–756.
[15] F. Goutenoire, O. Isnard, E. Suard, O. Bohnke, Y. Laligant, R. Retoux, Ph. Lacorre, *J. Mater. Chem.* **2001**, *11*, 119–124.
[16] F. Tietz, *Ionics* **1999**, *5*, 129–139.
[17] K. Huang, J. Wan, J. B. Goodenough, *J. Mater. Sci.* **2001**, *36*, 1093–1098.
[18] A. Atkinson, S. Barnett, R. J. Gorte, J. T. S. Irvine, A. J. McEvoy, M. Morgensen, S. C. Singhal, J. Vohs, *Nat. Mater.* **2003**, *3*, 17–27.
[19] F. Goutenoire, O. Isnard, R. Retoux, P. Lacorre, *Chem. Mater.* **2000**, *12*, 2575–2580.
[20] J. B. Goodenough, *Nature* **2000**, *404*, 821–822.
[21] P. Fischer, G. Frey, M. Koch, M. Könnecke, V. Pomjakushin, J. Schefer, R. Thut, N. Schlumpf, R. Bürge, U. Greuter, S. Bondt, E. Berruyer, *Phys. B* **2000**, *276–278*, 146–147.
[22] H. M. Rietveld, *J. Appl. Crystallogr.* **1969**, *2*, 65–71.
[23] J. Rodríguez-Carvajal, *Phys. B* **1993**, *192*, 55–69.

Received: March 7, 2011
Published Online: June 17, 2011

